



# Efficient Pd on carbon catalyst for ammonium formate dehydrogenation: Effect of surface oxygen functional groups

Zhun Dong<sup>a</sup>, Ahmad Mukhtar<sup>a</sup>, Thomas Ludwig<sup>b</sup>, Sneha A. Akhade<sup>b,\*</sup>, ShinYoung Kang<sup>b</sup>, Brandon Wood<sup>b</sup>, Katarzyna Grubel<sup>c</sup>, Mark Engelhard<sup>d</sup>, Tom Autrey<sup>c</sup>, Hongfei Lin<sup>a,\*</sup>

<sup>a</sup> Gene and Linda Voiland School of Chemical Engineering and Bioengineering, Washington State University, Pullman, WA 99163, United States

<sup>b</sup> Materials Sciences Division, Lawrence Livermore National Laboratory, Livermore, CA 94550, United States

<sup>c</sup> Physical Sciences Division, Pacific Northwest National Laboratory (PNNL), Richland, WA 99352, United States

<sup>d</sup> Environmental & Molecular Sciences, Earth & Biological Sciences, Pacific Northwest National Laboratory (PNNL), Richland, WA 99352, United States

## ARTICLE INFO

### Keywords:

Ammonium formate  
O-functional group  
Dehydrogenation  
LOHCs  
Palladium

## ABSTRACT

Formate solution is a promising liquid organic hydrogen carrier but suffers from kinetic challenges. This study investigates the kinetics of the surface-functionalized Pd on carbon catalysts for formate dehydrogenation and the impact of O-functional groups. The fraction of the distinguished O-functional groups was modulated by the different concentrated HNO<sub>3</sub> solutions treatment or by H<sub>2</sub> reduction. This study shows that the O-functional groups play critical roles in dispersing Pd nanoparticles and decreasing the activation energy for dehydrogenation. Density functional theory (DFT) calculation reveals that most O-functional groups enhance formate adsorption on the Pd active site. However, the existence of C=O groups consumes reducing agents and hinders the formation of metallic Pd. The electron transfer from Pd to oxygen functional groups is unfavorable to dehydrogenation. The as-prepared Pd5/re-ACA (reduced activated carbon washed by acid) exhibited significant activity with a higher turnover frequency of 13,511 h<sup>-1</sup> than commercial Pd/C.

## 1. Introduction

With increasing energy demands and growing concerns of environmental impact, there is increasing interest in the development of hydrogen energy sources because of no emission of pollutants and high energy density (~33 kWh/kg) [1–3]. Of particular interest for H<sub>2</sub> storage and delivery, some researchers are conducting investigations into the liquid organic hydrogen carriers (LOHCs) based on the advantages that 1) potentially carry more hydrogen; 2) more flexible and closely integrate with existing transportation infrastructures; 3) carry hydrogen at low-pressure and near ambient temperatures [4–6]. Formic acid (H<sub>2</sub>CO<sub>2</sub>) [7–9] and formate solution (MHCO<sub>2</sub>, M=Na<sup>+</sup>, K<sup>+</sup>, NH<sub>4</sub><sup>+</sup>) have been a very efficient medium among various LOHCs, especially ammonium formate (Fig. S1) [10–14]. The thermodynamics for H<sub>2</sub> release and uptake by formic acid and formate solution shown as reaction (1) and (2) (Table 1), shows that the Gibbs energy changes of formate solution are close to 0, indicating a much milder operation condition is required for formate solution working as a hydrogen carrier [2,15,16]. Although formate has a lower hydrogen density than formic acid, the advantage of

avoiding by-product CO poisoning attracts us to investigate formate-based hydrogen carriers and develop efficient catalysts for it [17,18].

Dehydrogenation of a formate solution may generate high-purity hydrogen with appropriate catalysts. For instance, noble metal-based heterogeneous catalysts have been well developed in the past decades. Our previous research has demonstrated that the Pd/C catalyst shows high activities for ammonium bicarbonate hydrogenation and ammonium formate dehydrogenation, making it superior to other noble metal-based catalysts (Ru/C, Rh/C, and Pt/C) [10]. Likewise, Koh et al. reported that N-doped carbon material derived from polyaniline (PANI) supported Pd nanoparticles (NPs) could efficiently catalyze the reversible reactions between sodium formate and bicarbonate (TOF of 2562 h<sup>-1</sup>). They mentioned that the pyridinic/pyrrolic N species formed on the graphitic carbon surfaces promoted the reversible formate/bicarbonate conversions by donating the electrons from N dopants to Pd active sites through a strong metal-support interaction [17]. Yao et al. developed g-C<sub>3</sub>N<sub>4</sub>-supported bimetallic Ag–Pd nanoparticles with various molar ratios via a facile co-reduction approach based on their

\* Corresponding authors.

E-mail addresses: [akhade1@llnl.gov](mailto:akhade1@llnl.gov) (S.A. Akhade), [hongfei.lin@wsu.edu](mailto:hongfei.lin@wsu.edu) (H. Lin).

<https://doi.org/10.1016/j.apcatb.2022.122015>

Received 12 June 2022; Received in revised form 19 September 2022; Accepted 21 September 2022

Available online 27 September 2022

0926-3373/© 2022 Elsevier B.V. All rights reserved.

**Table 1**

Thermodynamics of formic acid and formate solution up-taking and releasing H<sub>2</sub>.

Reactions	$\Delta_r G^0$ (kJ/mol)	H <sub>2</sub> density (g/L)	
H <sub>2</sub> CO <sub>2</sub> ↔ CO <sub>2</sub> + H <sub>2</sub>	-33	53	(1)
MHCO <sub>2</sub> + H <sub>2</sub> O ↔ MHCO <sub>3</sub> + H <sub>2</sub>	1	10–29	(2)

unique properties. Ag<sub>9</sub>Pd<sub>91</sub>/g-C<sub>3</sub>N<sub>4</sub> presented high activity with a TOF up to 480 h<sup>-1</sup> at 323 K. [19]. Shao et al. also reported the Pd nanoparticles supported mesoporous g-C<sub>3</sub>N<sub>4</sub> for formate-based reversible hydrogen storage and found that the transfer of electrons in the heterojunction from the semiconductor mesoporous g-C<sub>3</sub>N<sub>4</sub> enhanced the electron density of the metallic Pd and accelerated hydrogenation compared to the commercial Pd/C [20].

The surface O-functional groups may have some similar characteristics as N-doped groups. For example, 1) multiple N-C structures exist in the N-doped carbon materials (pyridinic N, pyrrolic N, and graphite N) [21,22]. Likewise, there are also several O-functional groups on the carbon support (carbonyl O, carboxylic O, ester O, hydroxyl O, etc.) [23, 24] 2) N-doping can increase the Pd concentration on the support surface, while the O-functional groups have the same effect. It was reported that the surface O-functional groups form anchoring sites for metallic precursors and metals, determining the properties of activated carbon as a catalyst support material [25–27]. For instance, the surface acidic O-functional groups decrease the hydrophobicity of the carbon, leading to the accessibility of the surface to aqueous metal precursors, while the less acidic groups increase the interaction between metal precursors with the support [25,28]. However, it is still unclear how the O-functional groups impact the ammonium formate dehydrogenation over Pd on carbon catalysts.

The most common technique to introduce O-functional groups onto the carbon surface is surface oxidation, including 1) refluxing of a single or a mixture of acid (HNO<sub>3</sub>, H<sub>2</sub>SO<sub>4</sub>) and an oxidizing agent (H<sub>2</sub>O<sub>2</sub>, KMnO<sub>4</sub>, and NaOCl); [29,30] 2) oxygen plasma treatment; [31,32] 3) irradiation of graphite with a high-energy electron beam [33]. In this study, we prepared various O-functionalized carbon-supported Pd catalysts. The fractions of distinguished O-functional groups were adjusted by acid refluxing using concentrated HNO<sub>3</sub> solutions or reduced under the H<sub>2</sub> atmosphere. We try to provide an in-depth understanding of the vital role of the surface O-functional groups in dispersing Pd nanoparticles, impacting the electron transfer during the reactions, changing the adsorption free energies of reactants, and adjusting the electronic conditions of Pd active sites.

## 2. Experimental section

### 2.1. Materials

The commercial Norit GSX activated carbon powder (steam activated, acid-washed), i.e., ACA, was purchased from Alfa Aesar (L11860); Nitric acid (69.0 %–70.0 %) and ammonium bicarbonate were purchased from J.T. Baker®; Sodium hydroxide (≥98 %), Ammonium formate (≥99.995 %), and Palladium(II) acetate (98 %) were purchased from Sigma Aldrich®.

### 2.2. Surface treatment of carbon supports

1 g ACA was added to a flask with 50 mL nitric acid solution at different concentrations, sonicating to form a uniform suspension. Then it was heated with reflux at 70 °C for 20 h. After the filtration, the ACA was washed with DI water and dried at 60 °C overnight. The Pd NPs were loaded on the ACA support by impregnation. Typically, the ACA supports treated with 0.4 M and 8 M HNO<sub>3</sub> solutions were marked as ACA0.4 and ACA8, respectively. The ACA support without any treatment was labeled as ACA. The H<sub>2</sub> reduction treatment was performed by

reducing the ACA support (labeled as re-ACA) in a tube furnace. 500 mg ACA was heated under the H<sub>2</sub> atmosphere at 500 °C for 2 h, with a temperature raising rate of 4 °C/min and a pure hydrogen gas flow rate of 60 mL/min.

### 2.3. Pd impregnation and reduction

250 mg ACA support after HNO<sub>3</sub> treatment (e.g., ACA0.4) was added into 20 mL acetone, followed by sonicating to form a uniform suspension. Then 26.4 mg Pd (II) acetate (5 % of nominal Pd loading) was dissolved into 20 mL acetone and mixed with ACA support suspensions. Stirred for 5 h until all acetone evaporated and then added 20 mL DI water to make a uniform suspension again. 20 mL aqueous NaBH<sub>4</sub> solution (0.059 mol/L) was added drop by drop into the previous suspension with continuous stirring and further stirred for 1 h at room temperature. After the filtration, the solids were washed with DI water and freeze-dried overnight. The final catalyst, e.g., Pd5/ACA0.4, was obtained, where Pd5 means 5% Pd loading.

### 2.4. Characterizations

The morphology and structure of the samples were analyzed by FEI Quanta 200 F field emission scanning electron microscope (SEM). Microstructural observations were performed with Thermo Fisher Scientific Themis Z 30–300 STEM operated at 300 kV. High-resolution imaging was performed in STEM mode, using a convergence angle of 25 mrad. A Micromeritics Auto Chem II system measured the temperature program decomposition (TPD) and CO pulse chemisorption. In a typical TPD measurement, around 30 mg of carbon materials were pre-treated at 200 °C with helium for 2 h to remove the adsorbed species. Following this, the helium gas flowed over the sample (20 mL/min) using a heating ramp of 10 °C/min until the maximum temperature of 750 °C was reached. The gases evolved were monitored by a thermal conductivity detector. For the CO pulse chemisorption, around 30 mg catalysts were pre-reduced in the 10 v% H<sub>2</sub>/Ar gas flow at 200 °C for 2 h, and then cooled to the room temperature. 10 v% CO/He was pulsed 20 times at room temperature and the CO profiles were monitored by thermal conductivity detector. The powder X-ray diffraction (XRD) was carried out on a Bruker D8 Advanced diffract meter under conditions of 40 kV and 40 mA for CuKα (λ = 0.15406 nm), with a scan range between 5–90° at the speed of 4° min<sup>-1</sup>. The X-ray photoelectron spectroscopy (XPS) measurements were performed using a Thermo Fisher NEXSA spectrometer with a 125 mm mean radius, full 180° hemispherical analyzer, and 128-channel detector. This system uses a focused monochromatic Al Kα X-ray (1486.7 eV) source for excitation and an electron emission angle of 60 degrees. The narrow scan spectra were collected using a pass-energy of 50 eV with a step size of 0.1 eV. For the Ag 3d5/2 line, these conditions produced an FWHM of 0.84 eV ± 0.02 eV. The binding energy (BE) scale is calibrated using the Cu 2p3/2 feature at 932.62 ± 0.05 eV and Au 4f7/2 at 83.96 ± 0.05 eV. The ATR-FTIR analysis was performed on the Bruker Tensor II spectrometer with a Harrick Horizon and a Harrick temperature controller ATC-024–4. A 2.89 mL liquid sampling cell with a ZnSe horizon trough (HON-LSP-J) was used to carry out the catalytic reactions.

### 2.5. Catalytic performance measurement

The formate dehydrogenation reaction experiments were carried out in a 50 mL Parr reactor. The gas outlet was connected to a NaOH solution trap (7 M) and then to an H<sub>2</sub> digital flowmeter (M-500SCCM-D-DB9M/CM from Alicat Scientific, Inc.). The NaOH trap was used to absorb CO<sub>2</sub> generated from bicarbonate decomposition, if applicable. Before reaction, the reactor was charged with N<sub>2</sub> gas for 5 min to ensure no O<sub>2</sub> was in the reaction system. After the set reaction temperature was reached, the released gas passed through the NaOH trap, and its volume was monitored using the H<sub>2</sub> flowmeter. The catalytic dehydrogenation

reaction was initiated by stirring the mixture of 0.05 g catalyst in 20 mL 1 M ammonium formate aqueous solution at 80 °C after N<sub>2</sub> purging. After the dehydrogenation reaction, the spent catalyst was collected back by filtration, washed with DI water three times, and freeze drying for 12 h. The stability test was carried out using spent catalysts in subsequent cycles with the same process. The hot filtration experiments were performed to study the impact of Pd leaching. In a typical dehydrogenation reaction, the catalyst was filtrated out after 10 min, and the filtrate was reloaded in the reactor and mixed with fresh reactant at the set temperature (80 °C). The gas product was tested by the H<sub>2</sub> flowmeter again.

## 2.6. Computational methods

Energy and charge density analysis calculations were performed using Density Functional Theory (DFT) in the projector-augmented wave formalism [34,35] using the code VASP [36–39]. The plane wave basis set energy cutoff of 400 eV was used, Gaussian smearing was used with a smearing width of 0.05 eV. Since relatively large simulation cells were adopted, only the gamma point was used to sample the Brillouin zone. Spin-polarized DFT calculations were performed for all geometry relaxations, except for computing the gas phase reference energy of hydrogen and formic acid. The RPBE functional [40] was employed with Grimme's zero damping DFT-D3 method [41,42] for van der Waals (vdW) corrections. Vibrational energy calculations were performed in VASP, and the thermochemistry module within the Atomic Simulation Environment (ASE) package [43]. Zero-point energies (ZPE) and free energy ( $\Delta G$ ) corrections for both adsorbates and gas-phase species were computed using the harmonic and ideal gas approximations.

The Pd/C catalyst interface with oxygen-based support modifications was constructed using a 55-atom Pd cluster and an O-based doped graphene sheet. Pristine graphene of size 29.69 × 30.00 Å consisting of 336 atoms was constructed and optimized using DFT. To incorporate oxygen functionalities, we introduced defects into the graphene sheet; subsequently, the defects were doped with the following functionalities and DFT-optimized, -O-, -OH-, -CHO-, and -COOH. The modified carbon supports are of size 29.69 × 25.71 Å and contain 16 defects, resulting in a defect surface area density of about  $2.1 \times 10^{14}$  defects / cm<sup>2</sup>. Under-coordinated C atoms as part of the defect were capped with hydrogen. A pre-optimized 55-atom Pd cluster from a previous study was adopted to represent approximately a 1.5–2.0 nm Pd nanoparticle (NP) [44]. The morphology of Pd NP was optimized using simulated annealed molecular dynamic simulations at 500 K with a 1 fs timestep using the embedded-atom method (EAM) [45] potential within the LAMMPS code [46]. The final structure was obtained via MD simulations using an NPT ensemble at 300 K and 1 bar within the EAM potential followed by DFT structural optimization. We refer the reader to our previous study for detailed information on the Pd NP preparation [44]. The Pd/C interface was constructed by mounting the optimized Pd NP onto various O-modified graphene sheets structural optimization. Finally, the supported nanoparticle structures were constructed by placing this nanoparticle near the carbon support surfaces. These structures were optimized using DFT and were used as starting structures for adsorption free energy and charge analysis calculations.

The adsorption free energies of hydrogen and formate were calculated on the Pd/O-modified graphene interface by evaluating the binding strength of hydrogen and formate on several high-symmetry binding sites of the Pd NP for each support. Hydrogen adsorption was evaluated on the three-fold face-centered cubic (FCC) and hexagonal-close-packed (HCP) hollow sites. Formate adsorption was computed with a bidentate configuration of formate wherein the formate oxygens were bound to neighboring on-top sites of Pd. For both molecules, the adsorption energies were computed for sites on the Pd NP near the support and those further away from the support. Charge density analysis was performed using the Bader scheme for charge partitioning [41,47–49].

## 3. Results and discussion

### 3.1. Catalyst characterization

The morphology of the as-prepared Pd5/ACA, Pd5/ACA0.4, Pd5/ACA8, and Pd5/re-ACA was characterized by TEM (shown in Fig. 1a–d, respectively). Obviously, Pd NPs are well-dispersed on the carbon support in all catalysts. After statistical calculation, the average diameter of Pd NPs supported on ACA is ~2.51 nm, and those of Pd5/ACA0.4 and Pd5/ACA8 catalysts are ~1.53 nm and ~1.15 nm, respectively, while the average Pd NPs size of Pd5/re-ACA is ~3.40 nm. The smaller Pd nanoparticles might result in higher Pd dispersion in Pd5/ACA catalysts (30.0% of Pd5/re-ACA vs. 45 % of Pd5/ACA8). Fig. 1e displays the corresponding element mapping and energy-dispersive X-ray spectrometry (EDX) of Pd5/re-ACA. It reveals the existence of C, O, and Pd elements. O atoms and Pd NPs are homogeneously dispersed on the carbon support. Fig. 1f and g represent the HRTEM images of Pd5/re-ACA and Pd5/ACA8, showing that part of the Pd elements was loaded in single atoms. A larger quantity of Pd single atoms was generated with a higher-concentration HNO<sub>3</sub> treatment of the ACA support, indicating O-functional groups are beneficial to improving the Pd dispersion with the formation of small nanoparticles, nanoclusters, and single-atoms. Fig. 1h shows the HRTEM image of the Pd5/ACA0.4 sample where the yellow square area is extended, as shown in Fig. 1i. The lattice distance of the particles is 0.223 nm, corresponding to Pd (111) structure [50].

The surface modification with functional groups changes the carbon surface's geometry and electronic environment, significantly affecting the adsorption of Pd NPs and thus changing the Pd particle sizes. The CO pulse chemisorption was used to measure Pd dispersion, as shown in Table S1. On the untreated ACA support, the Pd dispersion is 37%, which is higher than that of the commercial Pd/C (23%). The Pd dispersion increases with an increasing acid concentration on the ACA supports treated with various HNO<sub>3</sub> solutions. Interestingly, the Pd dispersion is 30 % for the Pd5/re-ACA catalyst, which is still higher than that of the commercial Pd/C catalyst. The results indicate that the surface oxygen-containing functional groups hinder the aggregation of Pd NPs and promote the formation of Pd single atoms.

The SEM images (Fig. S2) show that HNO<sub>3</sub> treatment obviously influences the Pd/ACA catalysts, especially carbon support morphologies. As shown in Fig. S2a, some small pores and defects are shown on the ACA carbon support surface. As the concentration of HNO<sub>3</sub> solution increases up to 0.4 M (Fig. S2b), more separate pores and defects are observed on the support. At the highest concentration to (8 M, Fig. S2c), some pores and defects are interconnected and form channels and larger defects on the catalyst. These defects introduced by the HNO<sub>3</sub> solution provide more anchoring sites, thus decreasing the Pd NPs' sizes and improving Pd dispersion simultaneously. The nitrogen adsorption-desorption isotherms of the ACA and ACA8 materials (Fig. S3) were performed to evaluate the pore size changed by HNO<sub>3</sub> oxidation. The feature type IV isotherms with H1-hysteresis (according to IUPAC classification) indicate the presence of uniform mesopores on the ACA and ACA8 carbon materials. The specific surface areas of ACA and ACA8 estimated by the Brunauer-Emmett-Teller (BET) method are 740 and 770 m<sup>2</sup>/g, and the pore sizes are 5.3 nm and 5.0 nm, respectively. The HNO<sub>3</sub> treatment is beneficial in optimizing the carbon microstructure to form narrow pores and enhance the specific surface area of the carbon support.

The XRD patterns of the ACA and the as-prepared ACA0.4 and Pd5/ACA0.4 samples were recorded to examine the crystal structures and phases, as shown in Fig. S4. The broad peaks at around 23° and 44° are assigned to amorphous carbon materials, and the sharp peaks at 26.6° correspond to carbon with graphitic structure (JCPDS No. 26-1079). No noticeable change could be found in the XRD pattern of ACA0.4 compared with ACA, suggesting an insignificant change in the bulk structure after the nitric acid treatment. After loading Pd, the barely visible peaks of the Pd species (JCPDS No. 46-1043) demonstrate that



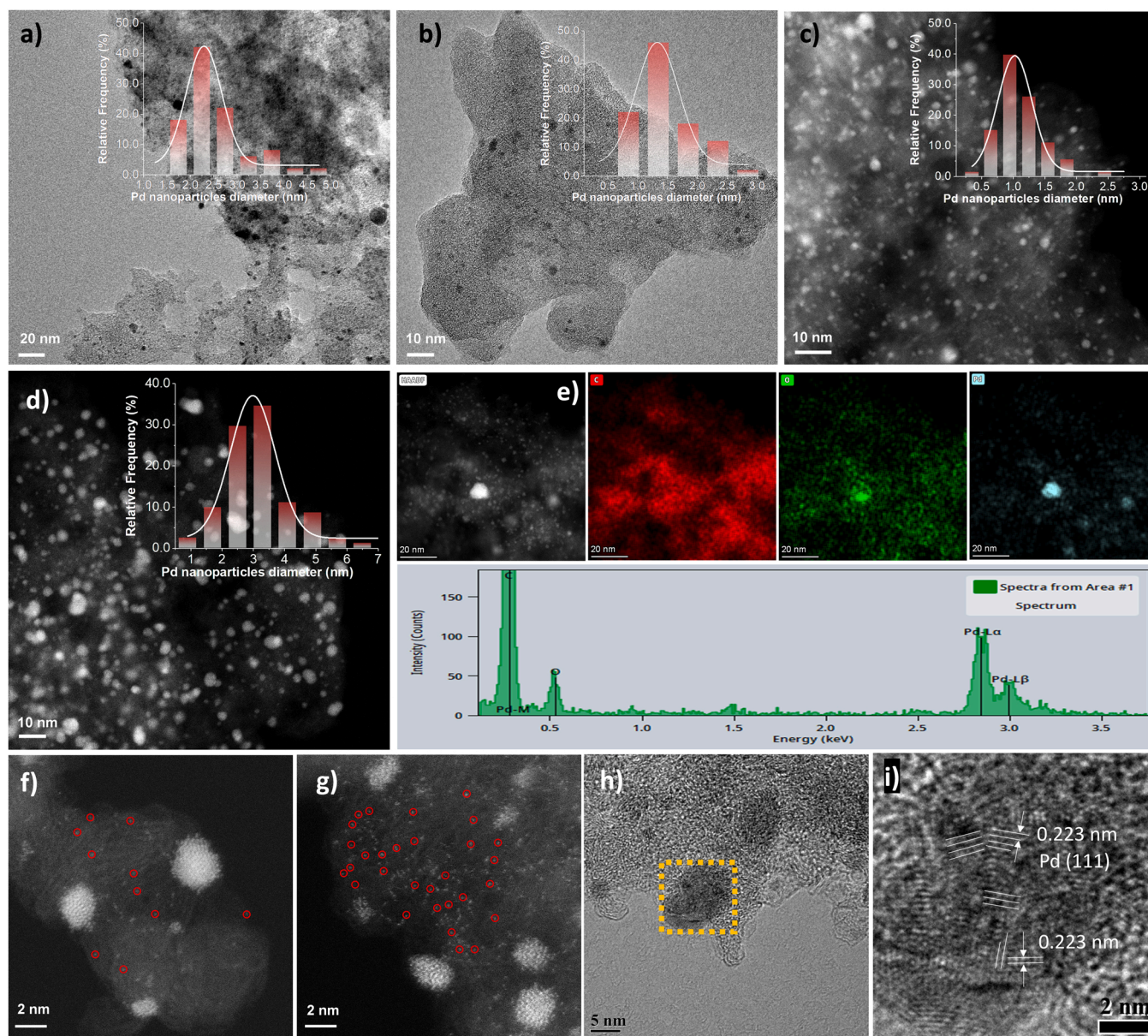


**Fig. 1.** TEM images of a) Pd5/ACA; b) Pd5/ACA0.4; c) Pd5/ACA8; d) Pd5/re-ACA; e) corresponding element mapping (red: carbon, green: oxygen, and light blue: palladium) and energy spectrum. HRTEM images of f) Pd5/re-ACA; g) Pd5/ACA8; h, i) Pd5/ACA0.4.

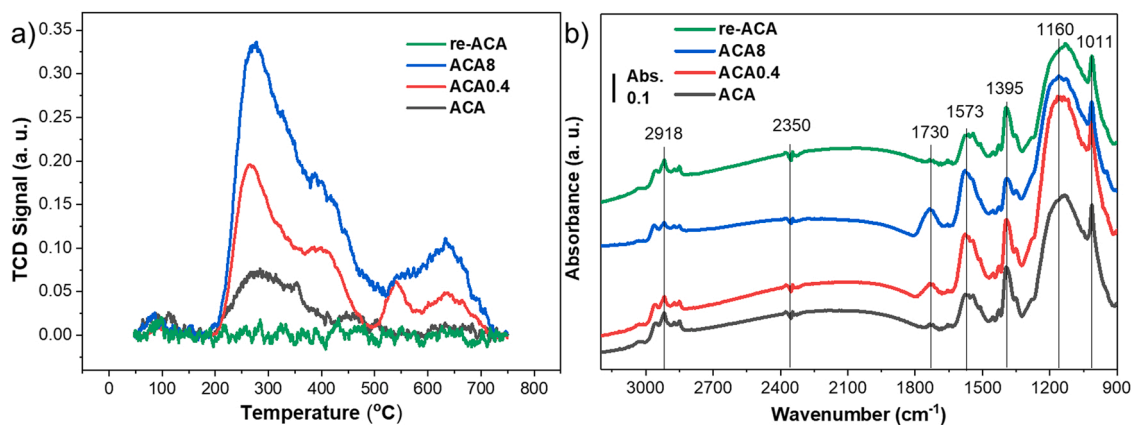


**Fig. 2.** a) TPD spectra, and b) ATR-IR spectra of ACA, re-ACA, ACA0.4, and ACA8 materials, and c) hydrogen volume versus reaction time of the Pd5/ACA8, Pd5/re-ACA8, and Pd5/re-ACA catalysts.

the Pd NPs were highly dispersed on the ACA0.4 support.

The  $\text{HNO}_3$  treatment could introduce different oxygen-containing functional groups on the carbon support surface [51–53]. TPD is one of the most used techniques to identify the surface functional groups on carbon materials, which decompose at different temperatures releasing  $\text{CO}$ ,  $\text{CO}_2$ , and  $\text{H}_2\text{O}$ . Fig. 2a displays the TPD results of the re-ACA, ACA, ACA0.4, and ACA8 carbon supports. Compared with the ACA sample, four apparent peaks are shown in the ACA0.4 and ACA8 samples at around 277 °C, 400 °C, 527 °C, and 647 °C, respectively, indicating multiple types of the surface O-functional groups were introduced into the ACA carbon support after the  $\text{HNO}_3$  treatment. Generally, the peaks at lower 630 °C are mostly acidic functional groups, such as carboxylic acid, lactol, lactone, and phenol groups. In contrast, the peaks at higher temperatures correspond to the basic functional groups, including quinones, carbonyl, ether, and ketones groups [54]. In this system, the peaks at 277 °C and 400 °C correspond to carboxylic and lactone groups, respectively. And the peaks at high temperatures (527 °C and 630 °C) are possibly related to phenol or anhydride groups [55,56]. With the ACA support treated with highly concentrated  $\text{HNO}_3$  (8 M), the TPD peak intensity of both acidic and basic O-functional groups was enhanced. Most carboxylic acid functional groups were removed when the ACA support was reduced in the  $\text{H}_2$  atmosphere at 500 °C for 2 h (re-ACA, green line in Fig. 2a).

Attenuated total reflectance infrared spectroscopy (ATR-IR) is another method employed to identify the surface functional groups on the carbon surface [51,57]. The FTIR spectra of the ACA support and those treated with various  $\text{HNO}_3$  solutions are shown in Fig. 2b. The peaks at 1011  $\text{cm}^{-1}$ , 1160  $\text{cm}^{-1}$ , and 1395  $\text{cm}^{-1}$  are related to the C-O bond stretching, which might be a C-O bond in ether or phenolic groups [58,59]. The broad peaks at 1573  $\text{cm}^{-1}$  and 1730  $\text{cm}^{-1}$  correspond to the C=O bond possibly derived from carboxyl groups (1710–1750  $\text{cm}^{-1}$ ), carbonyl groups (1560–1570  $\text{cm}^{-1}$  and 1700  $\text{cm}^{-1}$ ), and lactone (1710–1760  $\text{cm}^{-1}$ ) [60–62]. The weak peaks at 2350  $\text{cm}^{-1}$  are due to  $\text{CO}_2$  species adsorbed on the carbon surface [63]. The feature spectra at 2820–2950  $\text{cm}^{-1}$  are assigned to C-H stretching,

especially the peak at 2918  $\text{cm}^{-1}$  representing the C-H stretching in the carboxylic acid group [51,64]. The spectra change of the peaks at 1730  $\text{cm}^{-1}$  shows that the absorbance of the carbon samples is in the order of re-ACA < ACA < ACA0.4 < ACA8, suggesting that the carbon support treated with  $\text{HNO}_3$  at higher concentrations introduced more C=O bonds on the surface. On the other hand, the lowest C=O bond absorbance in the  $\text{H}_2$ -reduced ACA sample indicates that the surface functional groups containing the C=O bonds were reduced after the  $\text{H}_2$  reduction treatment.

The XPS analysis reveals that the Pd5/re-ACA, Pd5/ACA, Pd5/ACA0.4, and Pd5/ACA8 catalysts contain C, O, and Pd elements without other impurities (Fig. S5). Table S2 summarizes the surface element atomic fractions, indicating that the quantity of O atoms on the  $\text{HNO}_3$ -treated catalyst surface increases significantly (from 4.77 % to 9.13 % and 12.3 %) with increasing the  $\text{HNO}_3$  concentration. The  $\text{H}_2$ -reduction treatment efficiently removed the surface O-functional groups, showing the lowest O atomic fraction (3.21 %) in the Pd5/re-ACA sample. Besides, the Pd atomic fractions increased from 0.47 % to 0.91 % and 1.78 % in the Pd5/ACA, Pd5/ACA0.4, and Pd5/ACA8, respectively. And the comparable Pd atomic fractions in Pd5/re-ACA (0.53 %) and Pd5/ACA (0.47 %) suggest that the reduced O-functional groups after reduction did not result in a remarkable decrease in the surface Pd atomic fraction. In the high-resolution XPS spectra of O 1s (Fig. 3a), the asymmetric peaks suggest different forms of  $\text{O}^{2-}$  existing in three catalysts, Pd5/re-ACA, Pd5/ACA, and Pd5/ACA0.4. The peaks at 531.2 eV, 532.4 eV, and 533.6 eV are assigned to the unsaturated C=O bonds in carbonyl groups, saturated C-O bonds of hydroxyl groups, and -OH of hydroxyl groups, respectively. The O-H bonds at higher binding energy (535.9 eV) may correspond to chemisorbed  $\text{H}_2\text{O}$  on the catalyst surface [24,65]. Compared with Pd5/re-ACA and Pd5/ACA, Pd5/ACA0.4 shows enhanced C=O and -OH related peaks in Fig. 3a. It is consistent with the ATR-IR results (Fig. 2b) that the C=O stretching bond peak at 1730  $\text{cm}^{-1}$  was enhanced with the  $\text{HNO}_3$  treatment. Moreover, several new O-functional groups were detected in Pd5/ACA0.4, such as quinone (530.3 eV) and adsorbed oxygen (537.5 eV), resulting from the  $\text{HNO}_3$

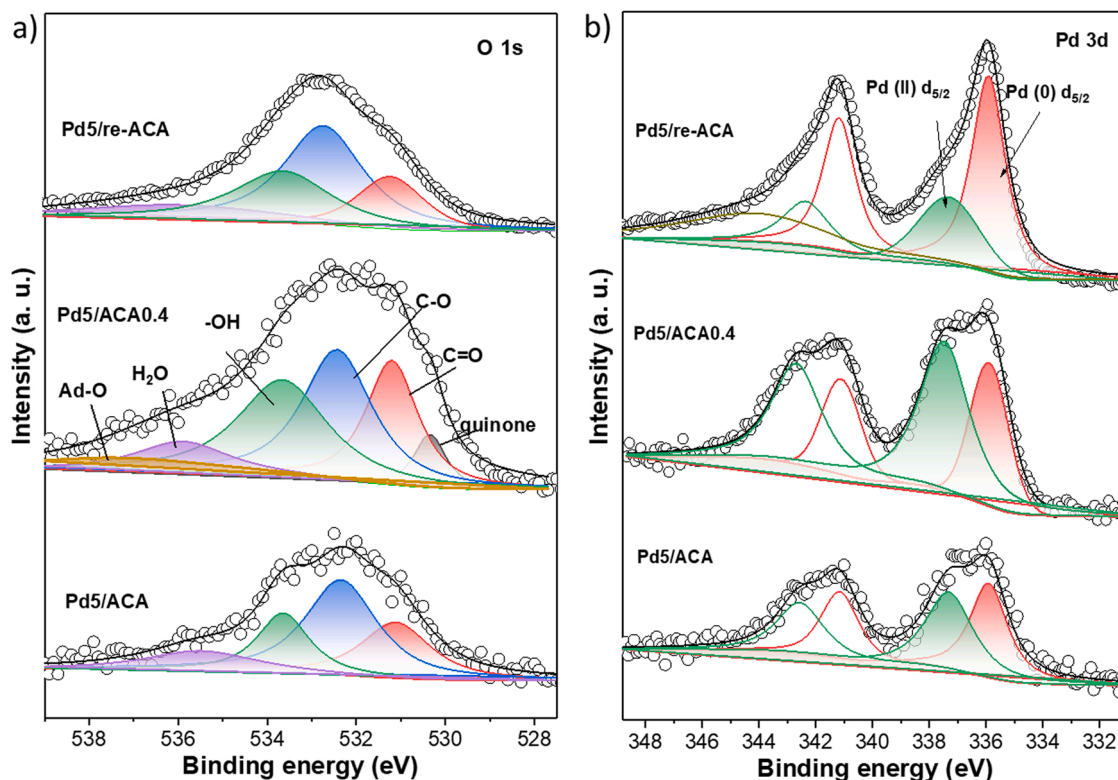


Fig. 3. XPS spectra of Pd5/ACA, Pd5/ACA0.4, and Pd5/re-ACA catalysts a) O 1s; 2) Pd 3d.



treatment [55,66].

Fig. 3b shows the Pd 3d spectra of Pd5/re-ACA, Pd5/ACA and Pd5/ACA0.4. Two main peaks associated with metallic Pd(0)  $3d_{5/2}$  and Pd(0)  $3d_{3/2}$  are located at 335.9 eV and 341.2 eV, respectively. Two peaks at higher binding energies (337.6 eV and 342.9 eV) correspond to the Pd (II) species [67,68]. The peak at 344.3 eV in Pd5/re-ACA sample is related to the satellite structure correlated to the electrons in the partially filled d orbitals [69]. The ratios of Pd(II)/Pd(0) in three samples were calculated using the peak areas of Pd  $3d_{5/2}$  [67], among which Pd5/ACA0.4 has the highest ratio of 1.95, followed by Pd5/ACA (1.02) and Pd5/re-ACA (0.55). Hence, a larger amount of positive Pd(II) ion species were on the HNO<sub>3</sub>-treated ACA support. Combining the ATR-IR results (Fig. 2b) and the XPS O 1 s spectra (Fig. 3a), it is assumed that more functional groups with C=O bonds were introduced onto the carbon support with the HNO<sub>3</sub> treatment, which would compete with the Pd precursor to be reduced during the catalyst synthesis. Accordingly, the Pd5/re-ACA has the lowest Pd(II)/Pd(0) ratio. Besides, the Pd (0)  $3d_{5/2}$  binding energies of Pd5/re-ACA and Pd5/ACA are 335.8 eV and 335.9 eV, respectively. They are slightly lower than that of Pd5/ACA0.4 (336.1 eV), suggesting that more intensive interaction between O-functional groups and Pd species on the HNO<sub>3</sub> treated carbon support.

### 3.2. Catalyst evaluation

To investigate how the surface O-functional groups impact formate dehydrogenation, we evaluated the activities of the Pd/ACA catalysts treated by different HNO<sub>3</sub> solutions. Fig. S6 shows that only a trace amount of CO<sub>2</sub> and no ammonia were detected in the gas phase products. Contrarily, hydrogen is the dominant gaseous product and

accounts for 99.6 v% (Table S3). As shown in Fig. 4a, under the same reaction conditions (0.05 g catalyst, 20 mL 1 M ammonium formate, 80 °C, 1 atm of N<sub>2</sub>, 40 min), the released H<sub>2</sub> volumes (or H<sub>2</sub> yields) over the Pd5/ACA, Pd5/ACA0.4, Pd5/ACA8, and Pd5/re-ACA catalysts are 349 mL (69 %), 333 mL (66 %), 307 mL (61 %), and 486 mL (96 %), respectively. They are higher than those over the commercial Pd/C (288 mL H<sub>2</sub> or 57% yield of H<sub>2</sub>). The Pd/ACA samples treated with various HNO<sub>3</sub> solutions did not improve the dehydrogenation activity significantly compared to the commercial Pd/C. The volume of released H<sub>2</sub> slightly declined with increasing the HNO<sub>3</sub> concentration. However, the Pd5/re-ACA catalyst, which the ACA support was reduced under an H<sub>2</sub> atmosphere, exhibited a higher initial reaction rate and higher hydrogen yield than the commercial Pd/C and the HNO<sub>3</sub>-treated Pd/ACA catalysts. Although Pd/re-ACA has slightly lower metal dispersion than the other catalysts (Table S1), the pre-reduction of the carbon support might lead to the formation of more metallic Pd uniformly dispersed throughout the carbon support. Therefore, the Pd active sites may be easily accessible to the reactant molecules, resulting in a higher initial reaction rate.

The effect of Pd loading is shown in Fig. S7, which indicates that higher loading of Pd provides more active sites for interacting with the reactant molecules. Therefore, the Pd/ACA catalysts with a 5 wt% Pd loading were chosen for further investigation. As shown in Table 1, the Pd5/re-ACA has a 1.6-fold higher turnover frequency (TOF), the detailed TOF calculation is shown in Supporting Information) of 13,511 h<sup>-1</sup> than the commercial Pd/C (8547 h<sup>-1</sup>). The TOFs of the Pd5/ACA, Pd5/ACA0.4, and Pd5/ACA8 are 7476 h<sup>-1</sup>, 6127 h<sup>-1</sup>, and 4304 h<sup>-1</sup>, respectively, suggesting that the HNO<sub>3</sub>-treated Pd catalysts show decreased activity with increasing the HNO<sub>3</sub> concentration. Indeed, the Pd5/re-ACA has a higher TOF than most Pd-based catalysts reported in

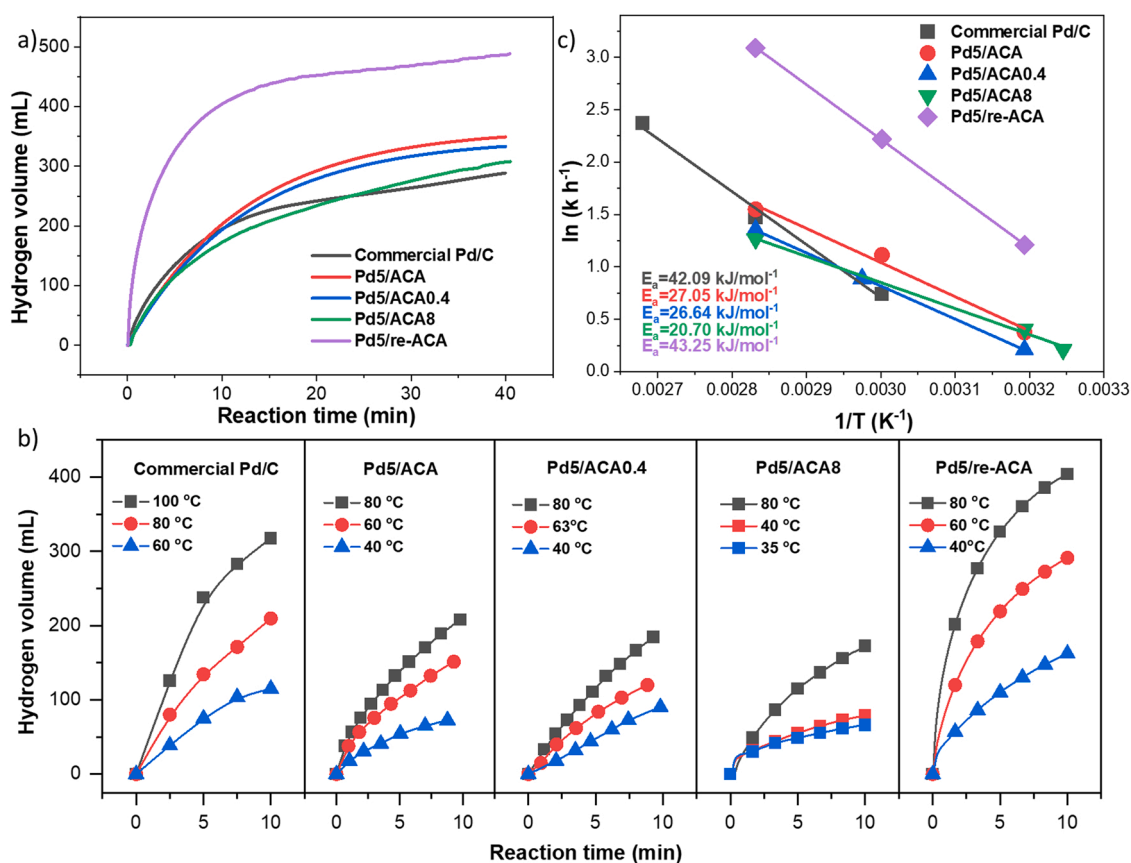


Fig. 4. Comparison of the dehydrogenation activity of the commercial Pd/C and various Pd/ACA catalysts. a) hydrogen volume versus reaction time (80 °C); b) effect of reaction temperatures for the formate dehydrogenation; c) Arrhenius plot (the initial reaction rates were averaged from 0 to 5 min). Reaction conditions: 0.05 g catalyst, 20 mmol ammonium formate, 1 atm of N<sub>2</sub>, 40 min.

the literature under comparable reaction conditions (Table 1). Some other research groups calculated TOF per unit of the total amount of loaded metal species. For comparison, the TOFs of the as-synthesized Pd/ACA catalysts were re-calculated based on the total amount of Pd. The results are summarized in Table 1, in which the TOFs are labeled with various superscripts to distinguish the different TOF calculation methods. The most active catalyst, Pd5/re-ACA, displays the highest TOF of  $4053 \text{ h}^{-1}$  per mole of total Pd loading or  $13,511 \text{ h}^{-1}$  per mole of surface Pd active sites, which are higher than the reported TOFs on various supported Pd catalysts in the literature using the same calculation methods. Besides, the TOF of Pd5/re-ACA at  $40^\circ\text{C}$  reached  $5472 \text{ h}^{-1}$  per mole of the surface Pd active sites, indicating its potential application at low temperatures. (Table 2).

The formate dehydrogenation mechanism was discussed based on a kinetic study. The power law kinetic model was utilized to describe the rate of hydrogen generation as a function of the concentration of ammonium formate (shown in Supporting Information). [11,78] Fig. S8 shows the reaction order of Pd5/ACA-catalyzed formate dehydrogenation is  $0.96 \pm 0.06$ , which could be treated as the first-order reaction. Besides, the kinetic rate measurements of the as-prepared catalysts were performed in the temperature range of  $35^\circ\text{C} - 100^\circ\text{C}$ , as shown in Fig. 4b, to obtain the corresponding Arrhenius plot (Fig. 4c). Accordingly, the calculated apparent activation energies ( $E_a$ ) of dehydrogenation on the catalysts were determined using the Arrhenius equation (shown in Supporting Information). Before measurements, it was confirmed that the system was not at thermodynamic equilibrium or in the mass transfer limiting region (Fig. S9). As shown in Fig. 4c, the  $E_a$  of Pd5/ACA, Pd5/ACA0.4, and Pd5/ACA8 were 27.1, 26.6, and  $20.7 \text{ kJ/mol}$ , respectively, lower than that of the commercial Pd/C ( $42.1 \text{ kJ/mol}$ ). Interestingly, the  $E_a$  of Pd5/re-ACA is  $43.3 \text{ kJ/mol}$ , slightly higher than that of commercial Pd/C. It suggests that the O-functional groups may decrease the energy barrier of the formate dehydrogenation reaction, but they do not significantly enhance the  $\text{H}_2$  production yield. In other words, the rate-limiting step over Pd5/ACA, Pd5/ACA0.4 and Pd5/ACA8 may not be sensitive to temperature as that over Pd5/re-ACA. From the Arrhenius plot, we also obtain the

pre-exponential factor. While  $E_a$  reveals the energy barrier, the pre-exponential factor is related to the entropy of activation of the reaction. In this study, Pd5/re-ACA has the highest  $E_a$ , but the pre-exponential factor is significantly higher than other catalysts and thus plays the dominant role. As a result, the overall reaction rate constant of Pd5/re-ACA is higher than those of the other catalysts.

To further understand the ammonium formate dehydrogenation mechanism, the reaction was carried out by in-situ ATR-IR spectroscopy, enabling the time-resolved monitoring of formate conversion and bicarbonate formation. Characteristic vibrations of ammonium formate and ammonium bicarbonate were assigned by recording spectra of the pure compounds (Fig. S10). The formate-specific bands are at  $1576$ ,  $1382$ , and  $1349 \text{ cm}^{-1}$ , while the peaks at  $1359$  and  $1303 \text{ cm}^{-1}$  are related to bicarbonate bond vibrations. The peak at  $1453 \text{ cm}^{-1}$  displayed in the FTIR spectra of both formate and bicarbonate samples corresponds to the bending of N-H bonds in ammonium cations. Fig. 5a shows the selected in-situ ATR-IR spectra recorded in the air at room temperature for 1 h of the formate conversion on the Pd5/re-ACA catalyst (shown in Fig. S11). At the initial stage, the specific peaks of formate can be observed at  $1576 \text{ cm}^{-1}$  and  $1382 \text{ cm}^{-1}$  after the catalyst film is rinsed by a 2 M ammonium formate aqueous solution. Besides, a weak peak related to bicarbonate species at  $1359 \text{ cm}^{-1}$  was also detected in the initial recording. It was attributed to such high activity of Pd5/re-ACA that can catalyze a part of the formate to bicarbonate at the very beginning. The peak at  $1403 \text{ cm}^{-1}$  corresponds to the C-O functional groups on the catalyst, as shown in Fig. 2b. The formate peaks at  $1576 \text{ cm}^{-1}$  and  $1382 \text{ cm}^{-1}$  decreased significantly after 9 min of reaction, while the bicarbonate peaks at  $1359 \text{ cm}^{-1}$  and  $1303 \text{ cm}^{-1}$  were enhanced simultaneously. Interestingly, the C-O stretching peak shows a 'Blue shift' from  $1403 \text{ cm}^{-1}$  to  $1397 \text{ cm}^{-1}$  that occurred at the beginning of the reaction (0–18 min) and stabilized after a half-hour reaction, suggesting that the C-O bonds were weakened during the dehydrogenation reaction. [79,80] Our control experiments show that the ATR-IR spectra of the pure Pd5/re-ACA catalyst display similar peaks to the re-ACA carbon support, with a C-O stretching peak at  $\sim 1395 \text{ cm}^{-1}$ , as shown in Fig. S12. Accordingly, the C-O stretching peak shifted instantaneously from  $1395 \text{ cm}^{-1}$  to  $1403 \text{ cm}^{-1}$  when the Pd5/re-ACA was rinsed by 2 M ammonium formate. As the formate dehydrogenation proceeds, the 'Blue-shift' of the C-O stretching peak indicates that the electrons leave the C-O bond, which is thus destabilized. Correspondingly, the bicarbonate feature signals show a 'Red-shift' with increasing the wavenumber from  $1350 \text{ cm}^{-1}$  to  $1359 \text{ cm}^{-1}$  during the reaction. [81,82] After a half-hour reaction, the peaks were maintained at  $1359 \text{ cm}^{-1}$  but with an increasing absorbance. It argues that the bicarbonate bonds are unstable at the initial reaction, and their electron density increases to form more stable bicarbonate species after the reaction. The synchronous changes of the 'Blue shift' of the formate bond and the 'Red-shift' of the bicarbonate bond might reveal that electrons transfer from the C-O bonds in formate to the bicarbonate species. Besides, the in-situ ATR-IR evaluation over Pd5/ACA8 was performed under the same conditions as Pd5/re-ACA, as shown in Fig. 5b. Initially, the formate peaks at  $1576 \text{ cm}^{-1}$  and  $1382 \text{ cm}^{-1}$  can be observed as the same as those over Pd5/re-ACA. With increasing the reaction time, these formate peaks decreased while the bicarbonate peaks at  $1356 \text{ cm}^{-1}$  and  $1303 \text{ cm}^{-1}$  were enhanced simultaneously. After a 1-hour reaction, the 'Blue shift' of C-O stretching peak from  $1400 \text{ cm}^{-1}$  to  $1397 \text{ cm}^{-1}$  and the 'Red shift' of bicarbonate species from  $1350 \text{ cm}^{-1}$  to  $1356 \text{ cm}^{-1}$  were detected clearly, which maintains the same trend as Pd5/re-ACA. All these in-situ ATR-IR characterization results reveal that the reaction pathways over Pd5/re-ACA are identical to the Pd5/ACA8. In addition, the wavenumber difference of 'Blue shift' and 'Red shift' over Pd5/ACA8 ( $\sim 3$  and  $\sim 6 \text{ cm}^{-1}$ , respectively) is less than those over Pd5/re-ACA ( $\sim 6$  and  $\sim 9 \text{ cm}^{-1}$ , respectively). The extent of the IR spectral shifts suggests that more extensive electron transfer between the adsorbed formate and bicarbonate may promote faster surface reactions on Pd5/re-ACA than on Pd5/ACA8. On the other hand,

**Table 2**

The catalytic activity of the different Pd-based catalysts for the formate dehydrogenation.

Catalyst	Substance	T ( $^\circ\text{C}$ )	TON	TOF ( $\text{h}^{-1}$ ) <sup>a</sup>	Ref.
Commercial Pd/C	$\text{NH}_4\text{HCO}_2$	80	2122	$8547^c$	1966 <sup>c</sup>
Pd5/ACA	$\text{NH}_4\text{HCO}_2$	80	2153	$7476^c$	2766 <sup>c</sup>
Pd5/ACA0.4	$\text{NH}_4\text{HCO}_2$	80	1762	$6127^c$	2573 <sup>c</sup>
Pd5/ACA8	$\text{NH}_4\text{HCO}_2$	80	1280	$4304^c$	1937 <sup>c</sup>
Pd5/re-ACA	$\text{NH}_4\text{HCO}_2$	80	2702	$13,511^c$	4053 <sup>c</sup>
		40	–	$5472^c$	1642 <sup>c</sup>
AgPd@NH <sub>2</sub> -UiO-66	$\text{HCO}_2\text{H}$	80	–	$893^d$	[70]
(Co <sub>6</sub> )Ag <sub>0.1</sub> Pd <sub>0.9</sub> /rGO	$\text{NaHCO}_2$ / $\text{HCO}_2\text{H}$	25	–	$453^d$	[71]
Pd/Al <sub>2</sub> O <sub>3</sub>	$\text{NH}_4\text{HCO}_2$	80	92	–	[10]
Au <sub>3</sub> Pd <sub>1</sub> /C	$\text{NaHCO}_2$ / $\text{HCO}_2\text{H}$	92	–	$407.5^c$	[72]
Pd/C	$\text{NaHCO}_2$ / $\text{HCO}_2\text{H}$	30	–	$2832^a$	[73]
Pd/rGO	$\text{NaHCO}_2$ / $\text{HCO}_2\text{H}$	25	–	$20.6^b$	[74]
Ag@Pd@TiOx (TTIP)/TiO <sub>2</sub>	$\text{NaHCO}_2$	75	820	$6499^b$	[75]
1Au1Pd/AC	$\text{NH}_4\text{HCO}_2$	40	–	$4200^e$	[11]
Pd/N,P-C	$\text{KHCO}_2$	80	–	$3248^c$	[76]
Pd/NH <sub>2</sub> -CNT	$\text{NaHCO}_2$ / $\text{HCO}_2\text{H}$	50	–	$8137^f$	[77]

<sup>a</sup> The TOFs were calculated by using  $\text{H}_2$  yield at different reaction times, a: 1 min; b: 5 min; c: 10 min; d: 20 min; e: not mentioned, and f: time reached a conversion of 20%. g: The TOFs were calculated based on the surface-active sites.

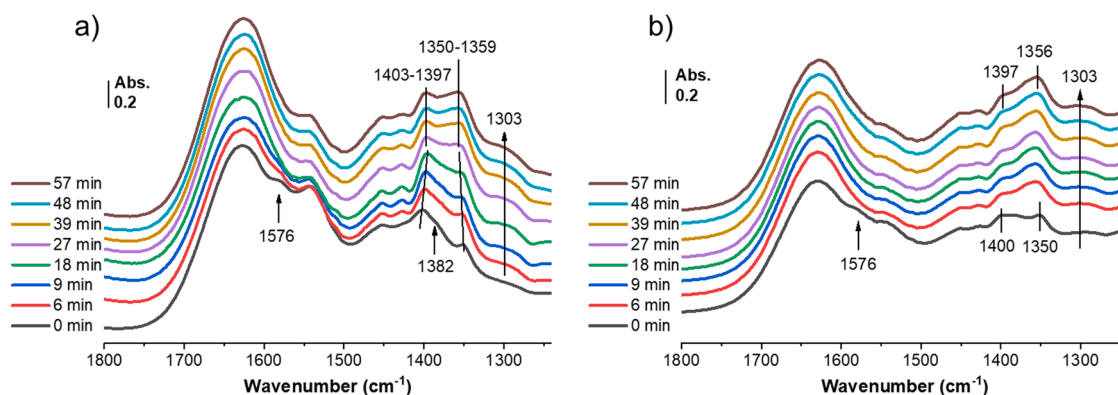


**Fig. 5.** Selected in-situ ATR-IR spectra on a) Pd5/re-ACA, b) Pd5/ACA8 catalyst as a function of time recorded after rinsing a 2 M ammonium formate solution to the spectral cell. The reference spectrum was recorded in the air before the rinse.

combining the TPD (Fig. 2a) and DFT simulation results (Fig. 10), the additionally introduced O-functional groups by  $\text{HNO}_3$  treatment on the ACA8 support attract more electrons transferring from Pd, resulting in the decline of electronic density around the Pd active sites and leading to the slower dehydrogenation reaction kinetics over Pd5/ACA8.

In addition, the stability tests were performed using the recycled Pd5/re-ACA catalysts (Fig. S13). We observed that the activities gradually decreased during the formate dehydrogenation reactions throughout five repeated cycles. The ICP-MS analysis of the spent Pd5/re-ACA (Table S1) and the hot filtration experiment (Fig. S14) revealed no Pd leaching during the reaction. The XPS spectra of the spent Pd5/re-ACA were compared with the fresh Pd5/re-ACA to elucidate the possible deactivation mechanism, as shown in Fig. S15. The O 1s spectra (Fig. S15a) display that the hydroxyl group fraction increases after formate dehydrogenation, which might be attributed to the adsorbed O-containing species during the reaction. The corresponding atomic element fractions of spent Pd5/re-ACA are summarized in Table S2. The fraction of the O-functional groups on the fresh and spent catalysts increases from 3.21% to 5.10%, respectively, suggesting that more surface O-containing species were formed after the reaction. Besides, both -OH and C-O bonds shifted to lower binding energy after the reaction, indicating the adsorbed O-containing species have a higher electron density and might change the surface electronic conditions. As shown in Table S2, the surface Pd atomic ratio of the fresh and spent catalysts increases from 0.53% to 0.80%, respectively, suggesting that the Pd NPs were segregated on the catalyst's outer surface. It is well accepted that Pd NPs are mobile and unstable on the carbon surface, resulting in aggregation and change of surrounding bonding conditions during the reaction, which may lead to deactivation. Fig. S15b shows that the Pd(II) fraction decreased after 5 reaction cycles. Most Pd species were reduced

to the metallic state since a large amount of  $\text{H}_2$  was generated during the reaction, which favorably reduced Pd(II) to Pd(0). Besides, the HRTEM images of the fresh and spent Pd5/re-ACA catalysts are shown in Fig. S16. The average Pd NPs size increases from 3.40 nm to 3.66 nm after 5 cycles of reaction. The slight growth of Pd NPs size may not be the main deactivation reason.

Furthermore, we selectively removed the specific O-functional groups on ACA8 and evaluated the formate dehydrogenation activity over the Pd/ACA8 catalysts. The reduced ACA8 was prepared by reducing the ACA8 carbon support in the  $\text{H}_2$  atmosphere at 300 °C (re-ACA8-300) or 500 °C (re-ACA8-500) for 2 h. The Pd impregnation and reduction methods are described in the Experimental section. Fig. 6a shows that hydrogen volume over Pd5/re-ACA8-500 is 450 mL (i.e.,  $\text{H}_2$  yield of 89%), which is higher than that over Pd5/re-ACA8-300 (435 mL,  $\text{H}_2$  yield of 86 %), Pd5/ACA8 (307 mL,  $\text{H}_2$  yield of 61 %), but lower than that over Pd5/re-ACA (486 mL,  $\text{H}_2$  yield of 96%). The TPD patterns of ACA8, re-ACA8-300, and re-ACA8-500 are shown in Fig. 6b. It displays that the carboxylate groups (corresponding to the TPD peak at  $\sim 277$  °C) were efficiently removed with the  $\text{H}_2$ -reduction at 300 °C or above. And the lactone groups (related to the TPD peak at  $\sim 400$  °C) were reduced in the  $\text{H}_2$  atmosphere at 500 °C. Compared with the Pd5/ACA8, the hydrogen yield of Pd5/re-ACA8-300 increases from 61 % to 86 %, indicating the reduction of carboxylate groups improves the catalyst activity dramatically. When we further reduced lactone groups, the hydrogen yield of Pd5/re-ACA8-500 improved slightly from 86 % to 89 %. It suggests that the lactone groups are not the dominant surface O-functional species that negatively impact the formate dehydrogenation kinetics. The  $\text{H}_2$  yields are lower on Pd5/re-ACA8-500 than Pd5/re-ACA (also reduced at 500 °C), 89 % vs. 96 %, because of the remaining phenol or anhydride groups on the re-ACA8-500 support. Hence, the

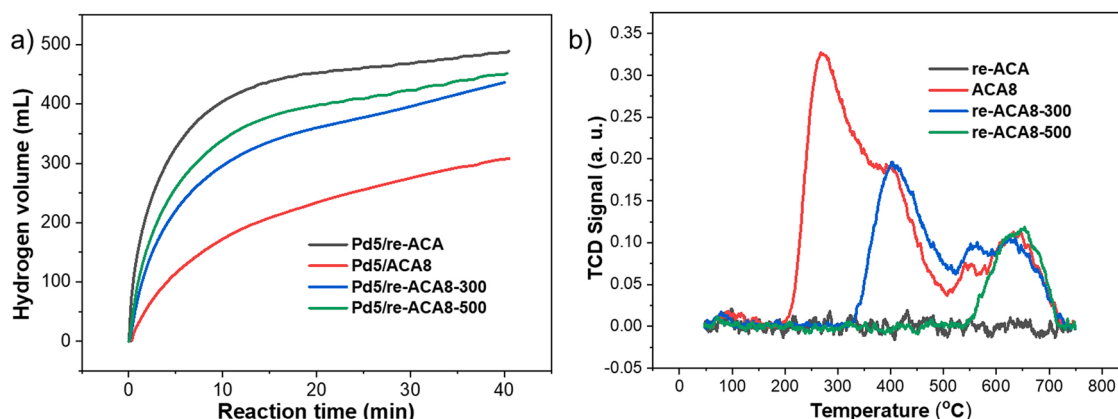


**Fig. 6.** a) hydrogen volume versus reaction time of the Pd5/ACA8, Pd5/re-ACA8, and Pd5/re-ACA catalysts; b) TPD patterns of ACA8 and re-ACA8 carbon supports.



carboxylic groups are the dominant carbon surface species limiting the formate dehydrogenation kinetics over Pd.

### 3.3. Density functional theory (DFT) calculation

To better understand the impact of O-containing functional groups on the Pd-based catalyst for dehydrogenation, we calculated the free energies of formate and hydrogen adsorbed on graphene-supported Pd NPs with DFT. The representative structures for adsorbed formate and hydrogen are displayed in Fig. 7. Based on the TEM results, the average Pd NP diameter of the as-prepared Pd/ACA is  $\sim 1.53$  nm, including approximately 55 Pd atoms in a Pd NP. Therefore, the impact from O-containing functional groups would be distinguished when the formate ions and hydrogen were adsorbed on different parts of the Pd NPs. We used two adsorption models, including near-to-support and far-from-support, as shown in Fig. 7. The DFT calculated adsorption free energies of formate and hydrogen on a binding site near to and far from each modified carbon support are displayed in Fig. 7 (The detailed calculated process is shown in Supporting Information).

As shown in Fig. 8, the adsorption free energy of the bidentate bound formate has a stronger variation ( $5 \text{ kJ/mol} > \Delta G_{\text{HCOO}^*} > -31 \text{ kJ/mol}$ ) than that of hydrogen ( $-22 \text{ kJ/mol} > \Delta G_{\text{H}^*} > -30 \text{ kJ/mol}$ ) due to the functionalization of the carbon support. The adsorption strength is correlated to the relative distance from the support. Indeed, the support effect is much more significant for binding sites closer to the support than for sites further away from the support. Furthermore, the support effect is much stronger for some adsorbates than others, as evidenced by the much more substantial effect on formate and negligible effect on hydrogen. Taking the graphene support as the reference, most O-containing groups strengthen the formate bonds with the Pd active site, except for the -CHO group near the support. This indicates that carbon supports modified by O-containing groups promote the adsorption of formate on the Pd surface. This preferential tuning of adsorption can be rationalized by evaluating the Pd NP's interfacial electronic and chemical properties and oxygen-modified carbon supports.

A fundamental understanding of the mechanism of the support effect described above would be helpful in engineering future supported catalysts for optimal performance. To investigate this, we focused on the interfacial charge transfer between the oxygen-modified carbon support and the Pd NPs. As shown in Fig. 9, the support modifications have a substantial effect on the total charge transfer between the nanoparticle and the support. Depending on the oxygen functionality, the interfacial charge transfer between the Pd NPs and carbon support spans a range of approximately  $1.5 e^-$  (where  $1 e^-$  is the charge of 1 electron). In all cases, there was a net negative charge transfer from the nanoparticle to the support, resulting in a partial positive charge on the nanoparticle or partial oxidation of the nanoparticle at the interface, as illustrated in the charge density isosurfaces in Fig. 10. Fig. 10 also shows that the charge transfer is localized near the nanoparticle-support interface rather than distributed evenly throughout the particle. This localized charge region

is the same region in which the support effect on adsorption free energies is the strongest, further emphasizing how catalyst-support interactions can play a crucial role in modulating the activity of formate adsorption and hydrogen release. Other factors, such as non-covalent interactions between the functional groups on the support and the adsorbed intermediates, may be important considerations in the rational design of supported catalyst systems. We note that hydrogen and formate were chosen as the adsorbates of interest in this study because they are hypothesized to be key intermediates in the overall formate dehydrogenation mechanism. Adsorbed formate is the result of formate in solution adsorbing oxygen-down in a bidentate mode onto the Pd surface, and the hydrogen adsorbate represents the final state for the dehydrogenation step from both formate and water, both of which provide hydrogen atoms in this process. The adsorbed hydrogen state is also the initial state for the final associative desorption step forming  $\text{H}_2$  gas. Future work is needed to understand the formate dehydrogenation mechanism in more detail. We also note that we do not directly calculate the reference energy of formate ion in solution using DFT; instead, we reference the energies for formic acid,  $\text{H}_2$ , and the fermi level of the catalyst, to the formate energy using experimental thermodynamic values and a thermodynamic cycle, as explained in the Supporting Information. This has been performed in a similar manner in previous work for other systems, such as nitrate adsorption, because of the difficulty in reliably calculating explicit ion adsorption steps in DFT [83]. Finally, we wish to note that this study utilizes a select number of adsorption sites with an emphasis on interfacial sites localized near the support. We have identified that the support modifications can have a significant effect on binding energies of formate. While the calculations do not rigorously account for all possible sites of adsorption available on the nanoparticle owing to the difficulty in exhaustively sampling all combinations of sites, support modification distributions, nanoparticle sizes, and other factors, the results do provide qualitative insights that the oxygen-based modifications on the support can affect the formate binding energies, and that these effects are enhanced near the support-particle interface. Further work would be required to obtain a quantitative estimation of these effects under various combinations of all the relevant factors.

It has been reported previously that an electron-rich Pd active site would be beneficial to promoting formate dehydrogenation. For example, Yin et al. reported that CeOx support efficiently promotes electron transfer from support to the metallic Pd-Ag active sites. And these electron-rich Pd-Ag sites facilitate the C-H activation process to generate more  $\text{H}_2$  from formic acid [84]. Contrarily, Zhang et al. studied the amine-groups impact on formic acid dehydrogenation. They found that the amine group as a proton scavenger could promote the O-H bond cleavage in formic acid [85]. Accordingly, the Pd5/ACA8 with plenty of COOH, CHO, and -O- groups on the carbon surface has more electrons transferred from the metallic Pd to the support, which accounts for the inferior activity. And the Pd5/re-ACA has a low atomic fraction of O species confirmed by XPS (Table S2). It is less affected by negative

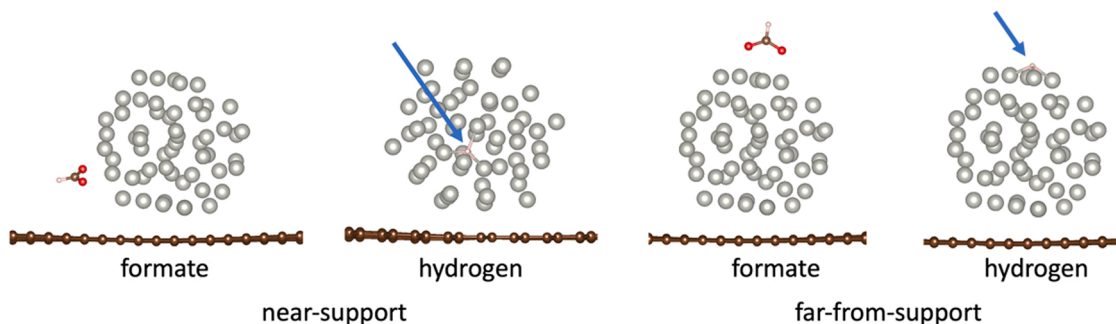
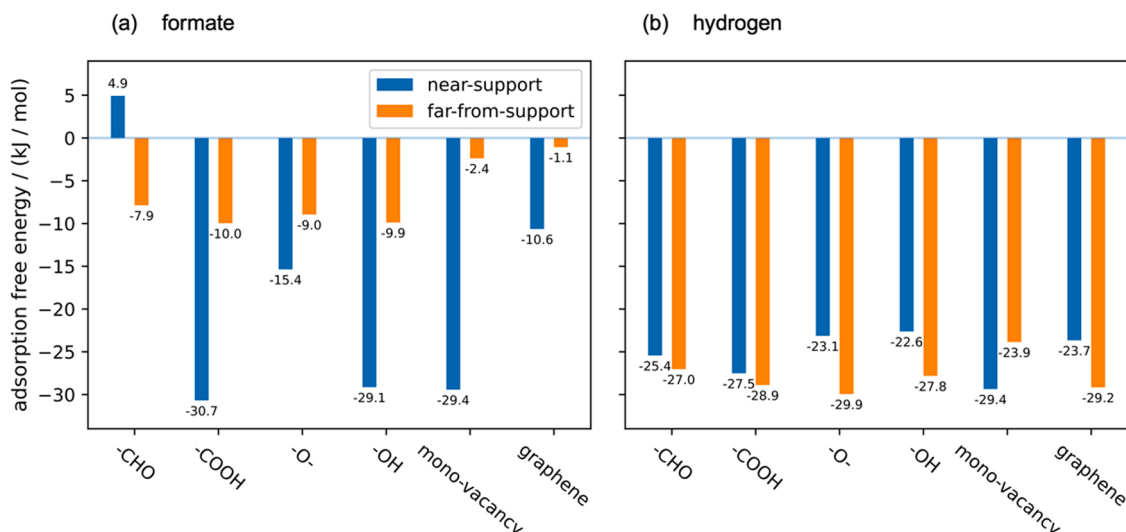
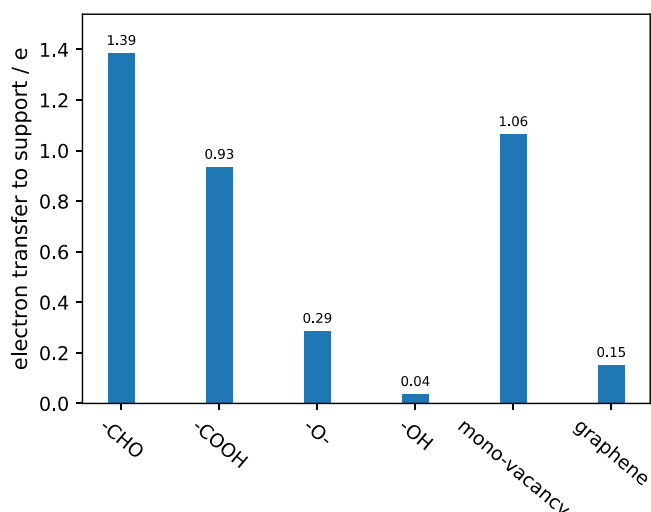


Fig. 7. Representative configurations for hydrogen and formate bound to positions near the support "near-to-support" and far from the support "far-from-support" on a Pd nanoparticle.



**Fig. 8.** Adsorption free energies of (a) formate and (b) hydrogen on Pd nanoparticles supported on surface functionalized carbon supports. Labels such as '-O-' indicate modification of the support, while the nanoparticle is approximately the same in all cases.



**Fig. 9.** Charge transfer between Pd nanoparticles and support for a variety of modified graphene supports. Positive values indicate net electron transfer from nanoparticle to support.

charge transfer but improved by positive effects of high dispersion and enhanced formate adsorption, consequently showing the highest TOF.

#### 4. Conclusion

In summary, we present a systematic study on the impact of the O-containing functional groups on the carbon-supported Pd catalysts for catalyzing ammonium formate ( $\text{NH}_4\text{HCO}_2$ ) dehydrogenation. The TOF

reaches  $13,511 \text{ h}^{-1}$  at  $80^\circ\text{C}$  on the Pd5/re-ACA catalyst and is 1.6-fold higher than the commercial 5% Pd/C. Furthermore, the concentrated  $\text{HNO}_3$  treatment can introduce more O-containing functional groups on the carbon support surface, especially with  $\text{C}=\text{O}$  bonds. On the one hand, these O-functional groups are beneficial to dispersing Pd NPs on the carbon support and efficiently decrease the activation energy for ammonium formate dehydrogenation. The DFT calculation reveals most O-functional groups enhance the formate adsorption on the Pd active sites. On the other hand, the surface functional groups containing  $\text{C}=\text{O}$  bonds consume the reducing agents and hinder the formation of metallic Pd. The carboxylic groups are the dominant surface O-functional species limiting the formate dehydrogenation kinetics over Pd active sites. The electron transfer from Pd to oxygen functional groups on the carbon support decreases the Pd catalyst activity. Contrarily, the exceptionally high dehydrogenation activity over Pd5/re-ACA suggests that precisely engineering the carbon surface to introduce a specific amount of selected O-functional groups could optimize the design of next-generation Pd on carbon catalysts.

#### CRediT authorship contribution statement

**Zhun Dong:** Conceptualization, Investigation, Writing - original draft. **Ahmad Mukhtar:** Writing - review & editing. **Thomas Ludwig:** Software, Writing - original draft. **Sneha A. Akhade:** Conceptualization, Writing - review & editing. **ShinYoung Kang:** Software. **Brandon Wood:** Resources. **Katarzyna Grubel:** Validation, Writing - review & editing. **Mark Engelhard:** Resources. **Tom Autrey:** Validation, Writing - review & editing. **Hongfei Lin:** Conceptualization, Funding acquisition, Supervision, Writing - review & editing.

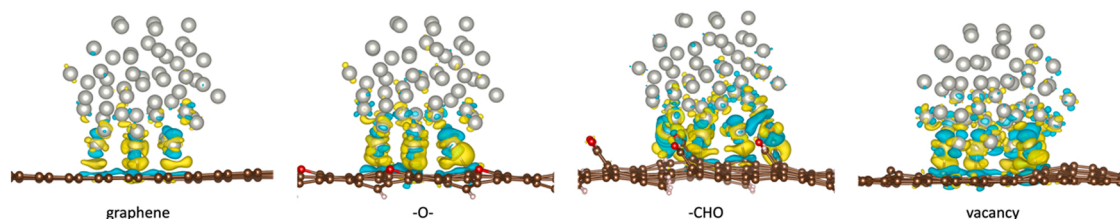


**Fig. 10.** Charge density isosurfaces with the nanoparticle-support charge transfer. The isosurfaces shown here correspond to charge density differences of  $\pm 0.002 \text{ Bohr}^{-3}$ . Yellow indicates regions of electron depletion, and cyan indicates regions of electron accumulation.

## Declaration of Competing Interest

The authors declare that they have no known competing financial interests or personal relationships that could have appeared to influence the work reported in this paper.

## Data Availability

Data will be made available on request.

## Acknowledgments

The authors thank for the support from the US Department of Energy, Office of Energy Efficiency and Renewable Energy, Fuel Cell Technologies Office, USA (Award No. DE-EE0008826). The XPS was performed on a project award (doi:10.46936/cpcy.proj.2020.51656/60000242) from the Environmental Molecular Sciences Laboratory, USA, a DOE Office of Science User Facility sponsored by the Biological and Environmental Research program under Contract No. DE-AC05-76RL01830. This work was performed under the auspices of the US Department of Energy by Lawrence Livermore National Laboratory, USA, under Contract DE-AC52-07NA27344. The authors acknowledge support from the Hydrogen Materials - Advanced Research Consortium (HyMARC), USA, established as part of the Energy Materials Network under the US Department of Energy, Office of Energy Efficiency and Renewable Energy, Hydrogen and Fuel Cell Technologies Office.

## Appendix A. Supporting information

Supplementary data associated with this article can be found in the online version at [doi:10.1016/j.apcatb.2022.122015](https://doi.org/10.1016/j.apcatb.2022.122015).

## References

- [1] R.M. Bullock, M.L. Helm, Molecular electrocatalysts for oxidation of hydrogen using earth-abundant metals: shoving protons around with proton relays, *Acc. Chem. Res.* 48 (7) (2015) 2017–2026, <https://doi.org/10.1021/acs.accounts.5b00069>.
- [2] K. Grubel, H. Jeong, C.W. Yoon, T. Autrey, Challenges and opportunities for using formate to store, transport, and use hydrogen, *J. Energy Chem.* 41 (2020) 216–224, <https://doi.org/10.1016/j.jechem.2019.05.016>.
- [3] D.Y. Shin, M.S. Kim, J.A. Kwon, Y.J. Shin, C.W. Yoon, D.H. Lim, Fundamental mechanisms of reversible dehydrogenation of formate on N-doped graphene-supported Pd nanoparticles, *J. Phys. Chem. C* 123 (3) (2019) 1539–1549, <https://doi.org/10.1021/acs.jpcc.8b07002>.
- [4] Z. Dong, A. Mukhtar, H. Lin, Heterogeneous catalysis on liquid organic hydrogen carriers, *Top. Catal.* 64 (7–8) (2021) 481–508, <https://doi.org/10.1007/s1244-021-01458-5>.
- [5] T. He, Q. Pei, P. Chen, Liquid organic hydrogen carriers, *J. Energy Chem.* 24 (5) (2015) 587–594, <https://doi.org/10.1016/j.jechem.2015.08.007>.
- [6] P. Preuster, C. Papp, P. Wasserscheid, Liquid organic hydrogen carriers (LOHCs): toward a hydrogen-free hydrogen economy, *Acc. Chem. Res.* 50 (1) (2017) 74–85, <https://doi.org/10.1021/acs.accounts.6b00474>.
- [7] W. Zhou, Z. Wei, A. Spannenberg, H. Jiao, K. Junge, H. Junge, M. Beller, Cobalt-catalyzed aqueous dehydrogenation of formic acid, *Chem. A Eur. J.* 25 (36) (2019) 8459–8464, <https://doi.org/10.1002/chem.201805612>.
- [8] A. Boddien, B. Loges, F. Gärtner, C. Torborg, K. Fumino, H. Junge, R. Ludwig, M. Beller, Iron-catalyzed hydrogen production from formic acid, *J. Am. Chem. Soc.* 132 (26) (2010) 8924–8934, <https://doi.org/10.1021/ja100925n>.
- [9] A. Boddien, Efficient dehydrogenation of formic, *Science* 323 (2011) 1733–1737.
- [10] J. Su, L. Yang, M. Lu, H. Lin, Highly efficient hydrogen storage system based on ammonium bicarbonate/formate redox equilibrium over palladium nanocatalysts, *ChemSusChem* 8 (5) (2015) 813–816, <https://doi.org/10.1002/cssc.201403251>.
- [11] K. Nakajima, M. Tominaga, M. Waseda, H. Miura, T. Shishido, Highly Efficient supported palladium-gold alloy catalysts for hydrogen storage based on ammonium bicarbonate/formate redox cycle, *ACS Sustain. Chem. Eng.* 7 (7) (2019) 6522–6530, <https://doi.org/10.1021/acssuschemeng.8b04698>.
- [12] J.F. Hull, Y. Himeda, W.H. Wang, B. Hashiguchi, R. Periana, D.J. Szalda, J. T. Muckerman, E. Fujita, Reversible hydrogen storage using CO<sub>2</sub> and a proton-switchable iridium catalyst in aqueous media under mild temperatures and pressures, *Nat. Chem.* 4 (5) (2012) 383–388, <https://doi.org/10.1038/nchem.1295>.
- [13] J.S. Yoo, F. Studt, F. Abild-Pedersen, J.K. Nørskov, Theoretical Analysis of Formic Acid Decomposition on Transition-Metal Catalysts. *Fuels Petrochemicals Div.* 2013 - Core Program Area 2013 AIChE Annu. Meet. Glob. Chall. Eng. a Sustain. Futur., 2013, pp. 299–300.
- [14] A. Boddien, C. Federsel, P. Sponholz, D. Mellmann, R. Jackstell, H. Junge, G. Laurenczy, M. Beller, Towards the development of a hydrogen battery, *Energy Environ. Sci.* 5 (10) (2012) 8907–8911, <https://doi.org/10.1039/c2ee22043a>.
- [15] K. Müller, K. Brooks, T. Autrey, Hydrogen storage in formic acid: a comparison of process options, *Energy Fuels* 31 (11) (2017) 12603–12611, <https://doi.org/10.1021/acs.energyfuels.7b02997>.
- [16] K. Müller, K. Brooks, T. Autrey, Releasing hydrogen at high pressures from liquid carriers: aspects for the H<sub>2</sub> delivery to fueling stations, *Energy Fuels* 32 (9) (2018) 10008–100015, <https://doi.org/10.1021/acs.energyfuels.8b01724>.
- [17] K. Koh, M. Jeon, D.M. Chevrier, P. Zhang, C.W. Yoon, T. Asefa, Novel nanoporous N-doped carbon-supported ultrasmall Pd nanoparticles: efficient catalysts for hydrogen storage and release, *Appl. Catal. B Environ.* 203 (2017) 820–828, <https://doi.org/10.1016/j.apcatb.2016.10.080>.
- [18] S. Enthaler, J. Von Langermann, T. Schmidt, Carbon dioxide and formic acid - the couple for environmental-friendly hydrogen storage? *Energy Environ. Sci.* 3 (9) (2010) 1207–1217, <https://doi.org/10.1039/b907569k>.
- [19] F. Yao, X. Li, C. Wan, L. Xu, Y. An, M. Ye, Z. Lei, Highly efficient hydrogen release from formic acid using a graphitic carbon nitride-supported AgPd nanoparticle catalyst, *Appl. Surf. Sci.* 426 (2017) 605–611, <https://doi.org/10.1016/j.apsusc.2017.07.193>.
- [20] X. Shao, Pd@C<sub>3</sub>N<sub>4</sub> nanocatalyst for highly efficient hydrogen storage system based on potassium bicarbonate/formate, *AIChE J.* 62 (7) (2016) 2410–2418, <https://doi.org/10.1002/aic.15218>.
- [21] Z. Dong, G. Liu, S. Zhou, Y. Zhang, W. Zhang, A. Fan, X. Zhang, X. Dai, Restructured Fe–Mn alloys encapsulated by N-doped carbon nanotube catalysts derived from bimetallic MOF for enhanced oxygen reduction reaction, *ChemCatChem* 10 (23) (2018) 5475–5486, <https://doi.org/10.1002/cctc.201801412>.
- [22] Q. Lai, J. Zheng, Z. Tang, D. Bi, J. Zhao, Y. Liang, Optimal configuration of N-doped carbon defects in 2D turbostratic carbon nanomesh for advanced oxygen reduction electrocatalysis, *Angew. Chem. Int. Ed.* 59 (29) (2020) 11999–12006, <https://doi.org/10.1002/anie.202000936>.
- [23] I. Gerber, M. Oubenali, R. Bacsá, J. Durand, A. Gonçalves, M.F.R. Pereira, F. Jolibois, L. Perrin, R. Poteau, P. Serp, Theoretical and experimental studies on the carbon-nanotube surface oxidation by nitric acid: interplay between functionalization and vacancy enlargement, *Chem. A Eur. J.* 17 (41) (2011) 11467–11477, <https://doi.org/10.1002/chem.201101438>.
- [24] W. Qi, W. Liu, B. Zhang, X. Gu, X. Guo, D. Su, Oxidative dehydrogenation on nanocarbon: identification and quantification of active sites by chemical titration, *Angew. Chem. Int. Ed.* 52 (52) (2013) 14224–14228, <https://doi.org/10.1002/anie.201306825>.
- [25] S.M. Senthil Kumar, J. Soler Herrero, S. Irusta, K. Scott, The effect of pretreatment of vulcan XC-72R carbon on morphology and electrochemical oxygen reduction kinetics of supported Pd nano-particle in acidic electrolyte, *J. Electroanal. Chem.* 647 (2) (2010) 211–221, <https://doi.org/10.1016/j.jelechem.2010.05.021>.
- [26] E. Auer, A. Freund, J. Pietsch, T. Tacke, Carbons as supports for industrial precious metal catalysts, *Appl. Catal. A Gen.* 173 (2) (1998) 259–271, [https://doi.org/10.1016/S0926-860X\(98\)00184-7](https://doi.org/10.1016/S0926-860X(98)00184-7).
- [27] F. Coloma, A. Sepúlveda-Escribano, J.L.G. Fierro, F. Rodríguez-Reinoso, Gas phase hydrogenation of crotonaldehyde over Pt/activated carbon catalysts. influence of the oxygen surface groups on the support, *Appl. Catal. A Gen.* 150 (1) (1997) 165–183, [https://doi.org/10.1016/S0926-860X\(96\)00301-8](https://doi.org/10.1016/S0926-860X(96)00301-8).
- [28] M.C. Román-Martínez, D. Cazorla-Amorós, A. Linares-Solano, C.S.M. de Lecea, Tpd and TPR characterization of carbonaceous supports and Pt/C catalysts, *Carbon* 31 (6) (1993) 895–902, [https://doi.org/10.1016/0008-6223\(93\)90190-L](https://doi.org/10.1016/0008-6223(93)90190-L).
- [29] X. Lu, W.L. Yim, B.H.R. Suryanto, C. Zhao, Electrocatalytic oxygen evolution at surface-oxidized multiwall carbon nanotubes, *J. Am. Chem. Soc.* 137 (8) (2015) 2901–2907, <https://doi.org/10.1021/ja509879r>.
- [30] K.A. Wepasnick, B.A. Smith, K.E. Schrote, H.K. Wilson, S.R. Diegelmann, D. H. Fairbrother, Surface and structural characterization of multi-walled carbon nanotubes following different oxidative treatments, *Carbon* 49 (1) (2011) 24–36, <https://doi.org/10.1016/j.carbon.2010.08.034>.
- [31] Y. Wang, Z. Jiang, Z. Yao, Formation of titania composite coatings on carbon steel by plasma electrolytic oxidation, *Appl. Surf. Sci.* 256 (20) (2010) 5818–5823, <https://doi.org/10.1016/j.apsusc.2010.03.038>.
- [32] C. Chen, A. Ogino, X. Wang, M. Nagatsu, Oxygen functionalization of multiwall carbon nanotubes by Ar/H<sub>2</sub>O plasma treatment, *Diam. Relat. Mater.* 20 (2) (2011) 153–156, <https://doi.org/10.1016/j.diamond.2010.11.018>.
- [33] J. Bai, H. Sun, X. Yin, X. Yin, S. Wang, A.E. Creamer, L. Xu, Z. Qin, F. He, B. Gao, Oxygen-content-controllable graphene oxide from electron-beam-irradiated graphite: synthesis, characterization, and removal of aqueous lead [Pb(II)], *ACS Appl. Mater. Interfaces* 8 (38) (2016) 25289–25296, <https://doi.org/10.1021/acsami.6b08059>.
- [34] D. Joubert, From ultrasoft pseudopotentials to the projector augmented-wave method, *Phys. Rev. B Condens. Matter Mater. Phys.* 59 (3) (1999) 1758–1775, <https://doi.org/10.1103/PhysRevB.59.1758>.
- [35] P.E. Blöchl, Projector augmented-wave method, *Phys. Rev. B* 50 (24) (1994) 17953–17979, <https://doi.org/10.1103/PhysRevB.50.17953>.
- [36] G. Kresse, J. Furthmüller, Efficiency of ab-initio total energy calculations for metals and semiconductors using a plane-wave basis set, *Comput. Mater. Sci.* 6 (1) (1996) 15–50, [https://doi.org/10.1016/0927-0256\(96\)00008-0](https://doi.org/10.1016/0927-0256(96)00008-0).
- [37] G. Kresse, J. Hafner, Ab initio molecular dynamics for liquid metals, *Phys. Rev. B* 47 (1) (1993) 558–561, <https://doi.org/10.1103/PhysRevB.47.558>.



- [38] G. Kresse, J. Hafner, Ab initio molecular-dynamics simulation of the liquid-metalamorphous- semiconductor transition in germanium, *Phys. Rev. B* 49 (20) (1994) 14251–14269, <https://doi.org/10.1103/PhysRevB.49.14251>.
- [39] G. Kresse, J. Furthmüller, Efficient iterative schemes for ab initio total-energy calculations using a plane-wave basis set, *Phys. Rev. B Condens. Matter Mater. Phys.* 54 (16) (1996) 11169–11186, <https://doi.org/10.1103/PhysRevB.54.11169>.
- [40] B. Hammer, L.B. Hansen, J.K. Nørskov, Improved adsorption energetics within density-functional theory using revised Perdew-Burke-Ernzerhof functionals, *Phys. Rev. B Condens. Matter Mater. Phys.* 59 (11) (1999) 7413–7421, <https://doi.org/10.1103/PhysRevB.59.7413>.
- [41] A. Allouche, Gabedit — a graphical user interface for computational chemistry softwares, *J. Comput. Chem.* 32 (2012) 174–182, <https://doi.org/10.1002/jcc.21600>.
- [42] S. Grimme, J. Antony, S. Ehrlich, H. Krieg, A consistent and accurate ab initio parametrization of density functional dispersion correction (DFT-D) for the 94 elements H-Pu, *J. Chem. Phys.* 132 (15) (2010), <https://doi.org/10.1063/1.3382344>.
- [43] A. Hjorth Larsen, J. Jørgen Mortensen, J. Blomqvist, I.E. Castelli, R. Christensen, M. Dulak, J. Friis, M.N. Groves, B. Hammer, C. Hargus, E.D. Hermes, P.C. Jennings, P. Bjerre Jensen, J. Kermod, J.R. Kitchin, E. Leonhard Kolsbjerg, J. Kubal, K. Kaasbjerg, S. Lysgaard, J. Bergmann Maronsson, T. Maxson, T. Olsen, L. Pastewka, A. Peterson, C. Rostgaard, J. Schiøtz, O. Schütt, M. Strange, K. S. Thygesen, T. Vegge, L. Vilhelmsen, M. Walter, Z. Zeng, K.W. Jacobsen, The atomic simulation environment - a python library for working with atoms, *J. Phys. Condens. Matter* 29 (27) (2017), <https://doi.org/10.1088/1361-648X/aa680e>.
- [44] D. Kim, J. Koh, S. Kang, T.W. Heo, B.C. Wood, E.S. Cho, S.M. Han, Chemomechanical effect of reduced graphene oxide encapsulation on hydrogen storage performance of Pd nanoparticles, *J. Mater. Chem. A* 9 (19) (2021) 11641–11650, <https://doi.org/10.1039/d1ta01240a>.
- [45] X.W. Zhou, J.A. Zimmerman, B.M. Wong, J.J. Hoyt, An embedded-atom method interatomic potential for Pd-H alloys, *J. Mater. Res.* 23 (3) (2008) 704–718, <https://doi.org/10.1557/jmr.2008.0090>.
- [46] S. Plimpton, Fast parallel algorithms for short-range molecular dynamics, *J. Comput. Phys.* 117 (1) (1995) 1–19, <https://doi.org/10.1006/JCPH.1995.1039>.
- [47] W. Tang, E. Sanville, G. Henkelman, A grid-based bader analysis algorithm without lattice bias, *J. Phys. Condens. Matter* 21 (8) (2009), <https://doi.org/10.1088/0953-8984/21/8/084204>.
- [48] M. Yu, D.R. Trinkle, Accurate and efficient algorithm for bader charge integration, *J. Chem. Phys.* 134 (6) (2011), <https://doi.org/10.1063/1.3553716>.
- [49] G. Henkelman, A. Arnaldsson, H. Jónsson, A fast and robust algorithm for bader decomposition of charge density, *Comput. Mater. Sci.* 36 (3) (2006) 354–360, <https://doi.org/10.1016/j.commatsci.2005.04.010>.
- [50] S.F. Ho, A. Mendoza-Garcia, S. Guo, K. He, D. Su, S. Liu, Ö. Metin, S. Sun, A facile route to monodisperse MPd (M = Co or Cu) alloy nanoparticles and their catalysis for electrooxidation of formic acid, *Nanoscale* 6 (12) (2014) 6970–6973, <https://doi.org/10.1039/c4nr01107d>.
- [51] M.S. Shafeyan, W.M.A.W. Daud, A. Houshmand, A. Shamiri, A review on surface modification of activated carbon for carbon dioxide adsorption, *J. Anal. Appl. Pyrolysis* 89 (2) (2010) 143–151, <https://doi.org/10.1016/j.jaap.2010.07.006>.
- [52] J.L. Figueiredo, M.F.R. Pereira, The role of surface chemistry in catalysis with carbons, *Catal. Today* 150 (1–2) (2010) 2–7, <https://doi.org/10.1016/j.cattod.2009.04.010>.
- [53] X. Zhang, B. Gao, A.E. Creamer, C. Cao, Y. Li, Adsorption of VOCs onto engineered carbon materials: a review, *J. Hazard. Mater.* 338 (2017) 102–123, <https://doi.org/10.1016/j.jhazmat.2017.05.013>.
- [54] M.A. Montes-Morán, D. Suárez, J.A. Menéndez, E. Fuente, On the nature of basic sites on carbon surfaces: an overview, *Carbon* 42 (7) (2004) 1219–1225, <https://doi.org/10.1016/j.carbon.2004.01.023>.
- [55] A. Stein, Z. Wang, M.A. Fierke, Functionalization of porous carbon materials with designed pore architecture, *Adv. Mater.* 21 (3) (2009) 265–293, <https://doi.org/10.1002/adma.200801492>.
- [56] S. Kundu, Y. Wang, W. Xia, M. Muhler, Thermal stability and reducibility of oxygen-containing functional groups on multiwalled carbon nanotube surfaces: a quantitative high-resolution Xps and TPD/TPR study, *J. Phys. Chem. C* 112 (43) (2008) 16869–16878, <https://doi.org/10.1021/jp804413a>.
- [57] A. Vimont, F. Thibault-Starzyk, M. Daturi, Analysing and understanding the active site by IR spectroscopy, *Chem. Soc. Rev.* 39 (12) (2010) 4928–4950, <https://doi.org/10.1039/b919543m>.
- [58] P.E. Fanning, M.A. Vannice, A DRIFTS study of the formation of surface groups on carbon by oxidation, *Carbon* 31 (5) (1993) 721–730, [https://doi.org/10.1016/0008-6223\(93\)90009-Y](https://doi.org/10.1016/0008-6223(93)90009-Y).
- [59] P.L. Walker, G. Tremblay, F.J. Vastola, Thermal desorption analysis of oxygen surface complexes on carbon, *Carbon* 16 (1978) 35–39.
- [60] W. Shen, Z. Li, Y. Liu, Surface chemical functional groups modification of porous carbon, *Recent Pat. Chem. Eng.* 1 (1) (2012) 27–40, <https://doi.org/10.2174/2211334710801010027>.
- [61] M.A. Lillo-Ródenas, D. Cazorla-Amorós, A. Linares-Solano, Behaviour of activated carbons with different pore size distributions and surface oxygen groups for benzene and toluene adsorption at low concentrations, *Carbon* 43 (8) (2005) 1758–1767, <https://doi.org/10.1016/j.carbon.2005.02.023>.
- [62] H.P. Boehm, Surface oxides on carbon and their analysis: a critical assessment, *Carbon* 40 (2) (2002) 145–149, [https://doi.org/10.1016/S0008-6223\(01\)00165-8](https://doi.org/10.1016/S0008-6223(01)00165-8).
- [63] K. Jiang, K. Xu, S. Zou, W. Cai, B-doped Pd catalyst: boosting room-temperature hydrogen production from formic acid – formate solutions, *J. Am. Chem. Soc.* 136 (2014) 4861–4864, <https://doi.org/10.1021/ja5008917>.
- [64] Z. Dong, W. Zhang, Y. Xiao, Y. Wang, C. Luan, C. Qin, Y. Dong, M. Li, X. Dai, X. Zhang, One-pot-synthesized CoFe-glycerate hollow spheres with rich oxyhydroxides for efficient oxygen evolution reaction, *ACS Sustain. Chem. Eng.* 8 (14) (2020) 5464–5477, <https://doi.org/10.1021/acssuschemeng.9b06579>.
- [65] H.R. Byon, B.M. Gallant, S.W. Lee, Y. Shao-Horn, Role of oxygen functional groups in carbon nanotube/graphene freestanding electrodes for high performance lithium batteries, *Adv. Funct. Mater.* 23 (8) (2013) 1037–1045, <https://doi.org/10.1002/adfm.201200697>.
- [66] J.H. Zhou, Z.J. Sui, J. Zhu, P. Li, D. Chen, Y.C. Dai, W.K. Yuan, Characterization of surface oxygen complexes on carbon nanofibers by TPD, XPS and FT-IR, *Carbon* 45 (4) (2007) 785–796, <https://doi.org/10.1016/j.carbon.2006.11.019>.
- [67] C. Zhang, Y. Li, H. He, Sodium promoted Pd/TiO<sub>2</sub> for catalytic oxidation of formaldehyde at ambient temperature, *Environ. Sci. Technol.* (48) (2014) 5816–5822.
- [68] S.P. Chenakin, G. Melaet, R. Szukiewicz, N. Kruse, XPS study of the surface chemical state of a Pd/(SiO<sub>2</sub> + TiO<sub>2</sub>) catalyst after methane oxidation and SO<sub>2</sub> treatment, *J. Catal.* 312 (2014) 1–11, <https://doi.org/10.1016/j.jcat.2014.01.008>.
- [69] G.L. Christensen, M.A. Langell, Characterization of copper palladium oxide solid solutions by X-ray diffraction, X-ray photoelectron spectroscopy, and auger electron spectroscopy, *J. Phys. Chem. C* 117 (14) (2013) 7039–7049, <https://doi.org/10.1021/jp310344r>.
- [70] S.T. Gao, W. Liu, C. Feng, N.Z. Shang, C. Wang, A Ag-Pd alloy supported on an amine-functionalized UiO-66 as an efficient synergetic catalyst for the dehydrogenation of formic acid at room temperature, *Catal. Sci. Technol.* 6 (3) (2016) 869–874, <https://doi.org/10.1039/c5cy01190f>.
- [71] Y. Chen, Q.L. Zhu, N. Tsumori, Q. Xu, Immobilizing highly catalytically active noble metal nanoparticles on reduced graphene oxide: a non-noble metal sacrificial approach, *J. Am. Chem. Soc.* 137 (1) (2015) 106–109, <https://doi.org/10.1021/ja511511q>.
- [72] X.T. Guo, J. Zhang, J.C. Chi, Z.H. Li, Y.C. Liu, X.R. Liu, S.Y. Zhang, Efficient dehydrogenation of a formic acid-ammonium formate mixture over Au 3 Pd 1 catalyst, *RSC Adv.* 9 (11) (2019) 5995–6002, <https://doi.org/10.1039/c8ra09534e>.
- [73] Y. Kim, S. Hoon Kim, H.C. Ham, D.H. Kim, Mechanistic insights on aqueous formic acid dehydrogenation over Pd/C catalyst for efficient hydrogen production, *J. Catal.* 389 (2020) 506–516, <https://doi.org/10.1016/j.jcat.2020.06.033>.
- [74] O. Grad, M. Mihet, M. Coros, M. Dan, M.D. Lazar, G. Blanita, Reduced graphene oxide modified with noble metal nanoparticles for formic acid dehydrogenation, *Catal. Today* 366 (August 2020) (2021) 41–47, <https://doi.org/10.1016/j.cattod.2020.08.009>.
- [75] S. Masuda, Y. Shimoyi, K. Mori, Y. Kuwahara, H. Yamashita, Interconversion of formate/bicarbonate for hydrogen storage/release: improved activity following sacrificial surface modification of a Ag@Pd/TiO<sub>2</sub> catalyst with a TiO<sub>2</sub> Xshell, *ACS Appl. Energy Mater.* 3 (6) (2020) 5819–5829, <https://doi.org/10.1021/acsaem.0c00744>.
- [76] X. Shao, X. Miao, T. Zhang, W. Wang, J. Wang, X. Ji, Pd nanoparticles supported on N- And P-Co-doped carbon as catalysts for reversible formate-based chemical hydrogen storage, *ACS Appl. Nano Mater.* 3 (9) (2020) 9209–9217, <https://doi.org/10.1021/acsnm.0c01830>.
- [77] Y. Kim, H. Lee, S. Yang, J. Lee, H. Kim, S. Hwang, S.W. Jeon, D.H. Kim, Ultrafine Pd nanoparticles on amine-functionalized carbon nanotubes for hydrogen production from formic acid, *J. Catal.* 404 (2021) 324–333, <https://doi.org/10.1016/j.jcat.2021.11.007>.
- [78] S. Behar, N.A. Gómez-Mendoza, M.Á. Gómez-García, D. Wierczyński, F. Quignard, N. Tanchoux, Study and modelling of kinetics of the oxidation of VOC catalyzed by nanosized Cu-Mn spinels prepared via an alginate route, *Appl. Catal. A Gen.* 504 (2015) 203–210, <https://doi.org/10.1016/j.apcata.2014.12.021>.
- [79] D. Ferri, T. Bürgi, A. Baiker, Chiral modification of platinum catalysts by cinchonidine adsorption studied by in situ ATR-IR spectroscopy, *Chem. Commun.* 1 (13) (2001) 1172–1173, <https://doi.org/10.1039/b102884g>.
- [80] S.D. Ebbesen, B.L. Mojet, L. Lefferts, In situ ATR-IR study of nitrite hydrogenation over Pd/Al<sub>2</sub>O<sub>3</sub>, *J. Catal.* 256 (1) (2008) 15–23, <https://doi.org/10.1016/j.jcat.2008.02.013>.
- [81] D. Ferri, T. Bürgi, A. Baiker, In situ ATR-IR study of the adsorption of cinchonidine on Pd/Al<sub>2</sub>O<sub>3</sub>: differences and similarities with adsorption on Pt/Al<sub>2</sub>O<sub>3</sub>, *J. Catal.* 210 (1) (2002) 160–170, <https://doi.org/10.1006/jcat.2002.3660>.
- [82] S.D. Ebbesen, B.L. Mojet, L. Lefferts, In Situ ATR-IR study of CO adsorption and oxidation over Pt/Al<sub>2</sub>O<sub>3</sub> in gas and aqueous phase: promotion effects by water and PH, *J. Catal.* 246 (1) (2007) 66–73, <https://doi.org/10.1016/j.jcat.2006.11.019>.
- [83] F. Calle-Vallejo, M. Huang, J.B. Henry, M.T.M. Koper, A.S. Bandarenka, Theoretical design and experimental implementation of Ag/Au electrodes for the electrochemical reduction of nitrate, *Phys. Chem. Chem. Phys.* 15 (9) (2013) 3196–3202, <https://doi.org/10.1039/c2cp44620k>.
- [84] B. Yin, E. Zhao, X. Hua, K. Wang, W. Wang, G. Li, T. Liu, Ultrafine PdAg nanoparticles immobilized on nitrogen-doped carbon/cerium oxide for superior dehydrogenation of formic acid, *New J. Chem.* 44 (5) (2020) 2011–2015, <https://doi.org/10.1039/c9nj05661k>.
- [85] S.L. Zhang, S.J. Li, J.Y. Wang, H.N. Shang, Y.X. Bai, J.S. Liang, Amine-functionalized carbon nanotubes supported NiAuPd nanoparticles as an efficient in-situ prepared catalyst for formic acid dehydrogenation, *Int. J. Hydrog. Energy* 46 (70) (2021) 34727–34736, <https://doi.org/10.1016/j.ijhydene.2021.08.063>.